Computational Identification of Transition-Metal Dichalcogenides for Electrochemical CO_2 Reduction to Highly Reduced Species Beyond CO and HCOOH

Sungwoo Kang, Suyeon Ju, Seungwu Han, and Youngho Kang*

Read Online

ACCESS | Metrics & More | Article Recommendations | SI Supporting Information

ABSTRACT: Practical CO_2 reduction (CO_2R) catalysts are desirable to have high selectivity for highly reduced products at small overpotentials and minimal activity for the hydrogen evolution reaction (HER). Herein, to find such catalysts, we investigate the CO_2R activities of anion vacancies of two-dimensional (2D) transition-metal dichalcogenides (TMDs) by first-principles calculations. For 38 TMDs found in experiments, we calculate free energies of intermediates along the pathways to C_1 products. In most TMDs, the steric hindrance of anion vacancies leads to the selective reduction of CO_2 to HCHO. Among them, we suggest ReS_2 and $ReSe_2$ as promising candidates having a low onset potential for CO_2R and high selectivity vs the HER. In addition, they allow further reduction of HCHO to highly reduced species. Detailed mechanism analysis shows that free energies of *OCHO and *H (* denotes adsorbates) can be descriptors for efficient evaluation of CO_2R activities. Given the importance of the geometrical constraints of vacancies for the CO_2R mechanism, our results will help identify potential CO_2R catalysts with vacancies that are electrochemically active.
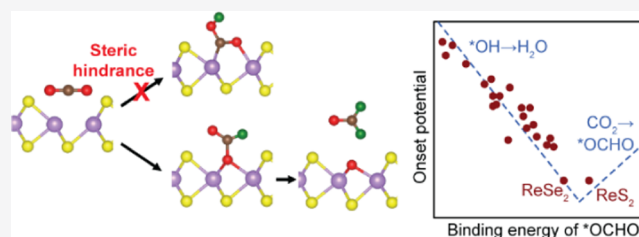
1. INTRODUCTION

The electrochemical carbon dioxide reduction (CO_2R) is receiving much attention as a promising method to convert CO_2 into valuable chemical fuels.[1] While CO_2R on most of known electrochemical catalysts produces simple C_1 species such as CO and HCOOH, production of highly reduced products such as methanol, ethylene, and 1-propanol can yield higher economic benefits.[2−4] Cu is a prototype CO_2R catalyst that has been extensively studied.[5−8] Cu can convert CO_2 to various products including multicarbon species like ethanol with high faradic efficiencies of ∼60%. However, the applied potential for producing such highly reduced products is fairly large on Cu [about −1 V vs reversible hydrogen electrode (RHE)], impeding wide utilization of Cu. Recently, nickel phosphides were found to selectively convert CO_2 to C_3 and C_4 species such as 2,3-furandiol as major CO_2R products at a low overpotential of 10 mV with a high faradic efficiency of 71%.[9] However, its catalytic activity declined rapidly with further increasing overpotential, limiting the maximum current density to less than 0.5 mA/cm². Therefore, high-performance CO_2R catalysts producing high-order carbon products are yet to be discovered.

Two-dimensional (2D) transition-metal dichalcogenides (TMDs) with chemical formula MX_2 (M = transition metals and X = S, Se, and Te), in particular MoS_2, are emerging candidates as electrochemical catalysts for diverse purposes like hydrogen evolution because of various merits such as earth abundance, high durability under acidic conditions, and low

costs.[10−13] In stable TMDs, pure basal planes are known to be largely inert while edges or vacancies serve as good active sites.[14,15] Recently, Francis et al. examined CO_2R products on MoS_2 and demonstrated that 1-propanol is produced as a main CO_2R product at reasonably small applied potentials (about −0.5 V vs RHE).[16] This result is very intriguing because C_3 species are rarely produced as a main CO_2R product on the known catalysts, especially at such small potentials, except for nickel phosphides. In a previous work, we investigated the CO_2R pathways of MoS_2 thoroughly using first-principles calculations, demonstrating that sulfur vacancies can serve as active sites for CO_2R reactions yielding 1-propanol.[17] We also revealed that the key mechanism for producing highly reduced species on MoS_2 is the condensation of HCHO that is one of the elementary CO_2R products.

Although the catalytic behavior of MoS_2 was studied theoretically and experimentally in the past, the faradic efficiency of the hydrogen evolution reaction (HER) on MoS_2 far exceeds that of CO_2R.[16,17] As a result, MoS_2 will not be practically attractive as long as the selectivity issue is not resolved. In this respect, it is worthwhile to examine other

TMDs for the superior selectivity of CO_2R against HER. Ji et al. examined CO_2R pathways to CO and CH_4 at anion vacancies of TMDs.[15] However, this work did not take into account pathways including the formation of *OCHO (* denotes a pure active site or an adsorbate) that would be favored at vacancies of TMDs compared to the *COOH formation (see below and ref 17.). Consequently, a question remains whether anion vacancies of other TMDs may serve as good active sites for CO_2R, possibly better than sulfur vacancies of MoS_2.

Here, we perform computational screening of TMDs to identify promising catalysts for efficient CO_2R using density functional theory (DFT) calculations. We focus on anion vacancy (V_X) as active sites for CO_2R reactions, as for MoS_2. Note that anion vacancies in TMDs are one of the native defects with low formation energies, and therefore, a moderate amount of V_X is always expected to be introduced in TMDs during synthesis.[18−26] In addition, V_X can be intentionally created in TMDs by plasma treatment,[27] electrochemical reduction,[28] and reaction with CO.[29] We study the free energies of intermediates that can be found in CO_2R pathways to CO, HCOOH, and HCHO for 38 TMDs. Based on these free energies, we show that most TMDs prefer the pathway to HCHO, which enables the formation of highly reduced species because of steric hindrance as well as high oxygen affinities at vacancy sites. Among the 38 TMDs, we suggest promising candidates such as ReS_2, $ReSe_2$, WTe_2, $CrSe_2$, and VSe_2 as potential CO_2R catalysts, and they are predicted to exhibit better catalytic performance than Cu. We also confirm that CO_2R pathways to C_2 products in ReS_2 and $ReSe_2$ are significantly downhill in energy at onset potentials that open the pathways to HCHO. Moreover, based on our data, we develop simple, but general descriptors for evaluating the catalytic performance of compounds with vacancies, which will help design new CO_2R catalysts enabling the evolution of highly reduced species.

2. METHOD

2.1. Computational Hydrogen Electrode (CHE) Model. To calculate the free energy of intermediates of CO_2R pathway, we employ the computational hydrogen electrode (CHE) model. The original CHE model applied to metal catalysts assumes concurrent addition of a proton−electron pair to the former adsorbate.[30] However, in defective semiconductors with localized levels around an active site, the electron transfer does not depend on the protonation step such that active sites can be charged by exchanging electrons with the electrode regardless of the adsorption of hydrogen. To take this point into account, we use the generalized CHE model in which the free energy of an intermediate $*C_xH_yO_z^q$ at potential U $[G^U(*C_xH_yO_z^q)]$ is given by[17,31]

$$G^U(*C_xH_yO_z^q) = E(*C_xH_yO_z^q) - E(*) - xG(CO_2)$$
$$- (2x + 0.5y - z)G(H_2)$$
$$- (z - 2x)G(H_2O)$$
$$+ (4x + y - 2z)eU - eqU$$
$$+ 0.059\,pH \times q + q\mu_{SHE}(e^-) + E_{add}$$

$$(1)$$

where $E(*)$ and $E(*C_xH_yO_z^q)$ are the DFT total energy of the bare catalyst and an adsorbate, respectively; $\mu_{SHE}(e^-)$ is the

electron energy of the standard hydrogen electrode: −4.44 eV on the absolute scale; and U is the applied potential referenced to RHE. Herein, pH is set to 7.[2] $G(CO_2)$, $G(H_2)$, and $G(H_2O)$ are the free energies of $CO_2(g)$, $H_2(g)$, and $H_2O(g)$, respectively. We consider a partial pressure of 1 atm for $CO_2(g)$ and $H_2(g)$ and room temperature. For $H_2O(g)$, we assume that it is in equilibrium with $H_2O(l)$ at room temperature, which leads to a vapor pressure of 3.49×10^{-2} atm. E_{add} is the additional energy term to convert the DFT energy of intermediates into free energy. It includes zero-point energy (ZPE), entropy, and average of vibrational energies obtained from heat capacity.[32] q is the most stable charge state of an adsorbate at a given U. It has a negative(positive) value if extra electrons are added into (removed from) the active site. While q should always be 0 for every intermediate on metallic catalysts or semiconductor catalysts without midgap states, it can have a nonzero value in defective semiconductor catalysts if defect-induced levels are presented between the gap.[17] The derivation of eq 1 is provided in the Supporting Information. (We provide free energies of all of the adsorbates in the neutral state, namely, $q = 0$, in Table S1 and charging energies in Table S2.) The importance of explicit consideration of the charging effect in the CHE model was recently highlighted by Zhao et al., who theoretically investigated CO_2R on Ni-doped graphene.[33]

We calculate the E_{add}'s in MoS_2 (Table S3) and consider them for the corresponding adsorbates in all of the TMDs, because E_{add} of an adsorbed species typically varies by less than 0.02 eV over different catalysts.[34,35] In the case of gaseous species (CO_2, CO, H_2, and H_2O), the ZPE is obtained using DFT calculations while entropy and heat capacity are taken from experimental data.[36] The free energies of products that are soluble in water [HCOOH(aq) and HCHO(aq)] are obtained by calculating the free energy of the corresponding molecule in the gas phase, assuming that they are in equilibrium with their aqueous states having an activity of 0.01.[32] For CO(g), we consider the correction energy (−0.45 eV), which is calculated using the same method as in a previous calculation,[32] to fix the error of DFT calculations in describing the triple bond of CO.

2.2. DFT Calculations. All DFT calculations are performed with the Vienna Ab initio Simulation Package (VASP).[37] The Perdew−Burke−Ernzerhof (PBE) exchange−correlation functional is used for describing the electron−electron interaction.[38] The plane-wave cutoff energy is set to 500 eV. Throughout this work, spin-polarized calculations are carried out. Atomic structures are relaxed until atomic forces acting on each atom are reduced under 0.03 eV/Å; 4 × 4 supercells of monolayer TMDs are employed, and 5 × 5 × 1 k-point mesh is used to sample Brillouin zone (BZ). We remove one chalcogen atom (X) in the supercell to create a V_X, which corresponds to 6.25% of concentration. For TMDs with local magnetic moments (VS_2, VSe_2, VTe_2, $CrSe_2$, and $CrTe_2$), we consider the ferromagnetic spin configuration for simplicity. For Au(111), Cu(111), and Sn(110) surfaces, we use 3 × 3 supercells for the first two and a 4 × 2 supercell for the last, including three atomic layers each, and use 3 × 3 × 1 k-point mesh for BZ sampling. About 15 Å of vacuum region is inserted into all supercells to avoid spurious interactions between periodic atomic images within the periodic boundary condition. The solvation energy of an intermediate is calculated using implicit solvation model[39] with parameters of 78.4 (dielectric constant), 0.6 Å (cavity width), 0.525 meV/
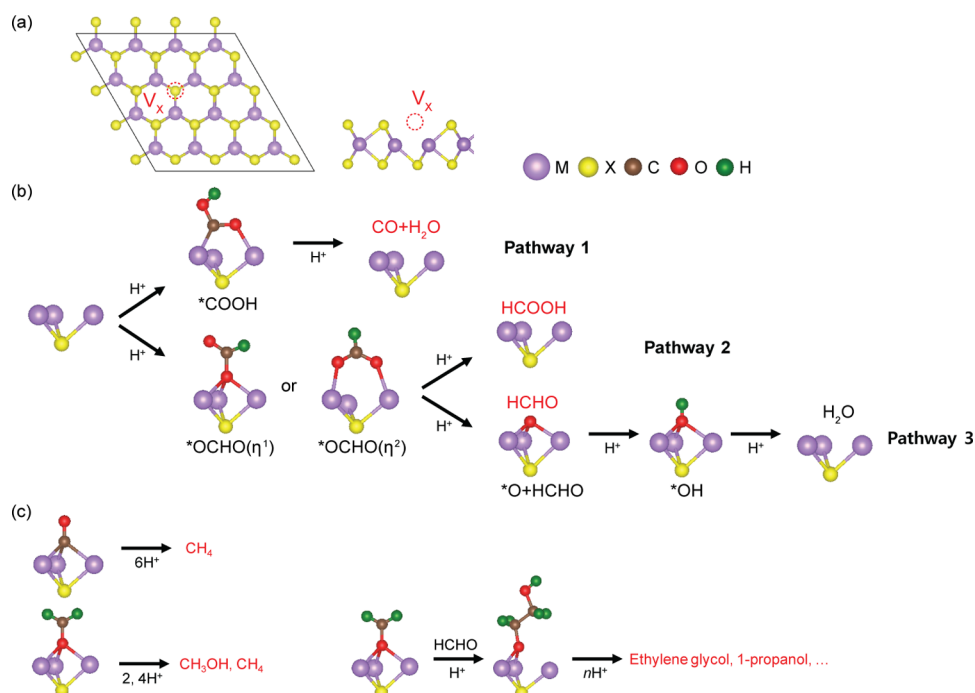
Figure 1. (a) Atomic structure of a vacancy site of MX_2, where M and X stand for transition metal and chalcogen element, respectively. (b) C_1 pathways to CO (pathway 1), HCOOH (pathway 2), and HCHO (pathway 3). (c) Possible reaction pathways opened by the further reduction of CO (top) and HCHO (bottom) at X-vacancy.

Å^2 (surface tension), and 0.0025 Å^{-3} (cutoff charge density). D2 scheme is employed to account for van der Waals interactions.[40] The formation energy of V_X (E_f) is calculated as follows

$$E_f = E(V_X) - E(\text{crystal}) + \mu_X \qquad (2)$$

where $E(\text{crystal})$ and $E(V_X)$ are the total energy of a clean TMD supercell and a supercell including one V_X. μ_X is the chemical potential of X, which is determined considering standard corrosion resistance of X.[14,41] The calculated E_f's of V_X in TMDs are listed in Table S4.

3. RESULTS AND DISCUSSION

3.1. Computational Screening. To screen potential 2D TMD catalysts for CO_2R, we first search for inorganic compounds with the chemical composition of MX_2 (M = transition metals and X = S, Se, and Te) from Inorganic Crystal Structure Database.[42] Among them, we consider only compounds with sixfold coordinated M atoms like MoS_2. MX_2 can have various phases like H, T, T′, and T″ phases. Herein, we adopt the most stable phase for each TMD. Ruling out TcS_2, in which Tc is radioactive, and CrS_2, whose pure phase is known to be hardly obtained, we choose 38 materials that were experimentally identified.[14] For all of the TMDs considered in the present work, we present information on phases, electrical properties (metal vs semiconductor), and positions of V_X levels in Table S4.

Figure 1a shows the atomistic structure of vacancy site of MX_2, and Figure 1b shows three possible reaction pathways to elementary C_1 products that can occur at V_X sites of 2D TMDs.[17] In pathway 1, CO_2 in solution is reduced to *COOH at the initial protonation step, yielding CO as a product. Meanwhile, the first intermediate can be *OCHO producing HCOOH (pathway 2) and HCHO (pathway 3). Resorption of CO and HCHO at V_X can lead to the formation of other C_1

products like CH_4, CH_3OH, and multicarbon species, as depicted in Figure 1c. We focus on pathways 1−3 in the following discussions because the primary goal here is not to predict the final products precisely, but to suggest catalysts with a good CO_2R selectivity relative to HER as well as a low onset potential to open reaction pathways for CO_2R. Such issues can be addressed by considering pathways 1−3; reduction steps beyond the formation of HCHO to form highly reduced species are known to be more energetically benign than the prior ones[17] (also see Section 3.2). On the other hand, the coupling between CO molecules at active sites, which is suggested to produce C_2 or C_3 species on Cu surfaces,[43−46] is unlikely to happen at V_X of TMDs because carbon atoms in CO are not exposed to the surface. Therefore, only C_1 species such as CH_4 and CH_3OH are possible to be formed by the further reduction of CO.

Considering the site-blocking effect, the preferred reaction pathway would be determined by comparing the free energy between competing intermediates at 0 V vs RHE.[17,32,47−49] This approach successfully predicted the major CO_2R products on the RuO_2 and Cu surface.[32,47] Thus, if $G^0(*OCHO)$ is lower than $G^0(*COOH)$, we assume that this reaction proceeds through pathway 2 or 3 rather than pathway 1. Similarly, the relative preference between pathways 2 and 3 is assessed by comparing $G^0(*+HCOOH(aq))$ and $G^0(*O+HCHO(aq))$. This criterion was applied to discover the preferred CO_2R pathways in MoS_2.[17] Nonetheless, if the energy difference between competing intermediates is small, then both pathways may play a role. On the other hand, when determining the favorable pathway, we pay attention to the difference in free energies at 0 V. However, the free-energy difference can change depending on the electrode potential in the case of semiconducting TMDs with localized in-gap states when q differs between competing intermediates (see eq 1 and Figure S1). As a result, different preferred pathways may

appear while the potential decreases. However, we confirmed that comparing free energies at 0 V is still valid in predicting preferred CO_2R pathways in such semiconducting TMDs for a wide range of potentials; the favorable pathway predicted at 0 V is maintained until about −0.8 V (Figure S1). In $MoSe_2$, $MoTe_2$, and WS_2, the preferred pathways can be changed at negatively large potentials below −0.8 V, compared to those at 0 V.

For *OCHO, there are two possible configurations which are denoted as η^1 and η^2 in Figure 2a. Between them, we find
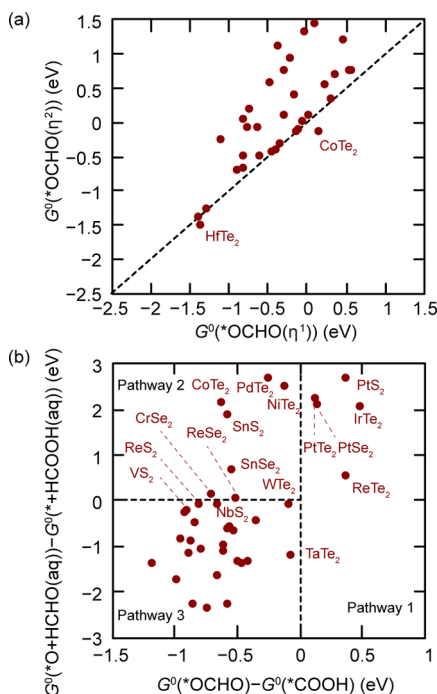
Figure 2. (a) Comparison of free energies of *OCHO(η^1) and *OCHO(η^2). (b) Free-energy differences between competing intermediates for the first and second protonation steps.

that *OCHO(η^1) is much more stable than *OCHO(η^2) in most TMDs, except for $CoTe_2$ and $HfTe_2$. This larger preference of *OCHO(η^1) originates from the structural feature of active sites. Namely, the bowl shape of V_X sterically hinders the simultaneous adsorption of two atoms at one vacancy site because it would cause significant distortions of the lattice around the vacancy site.[17,50] Including *OCHO, all of the geometries of intermediates examined in the present work are provided in the Supporting Information (see Figures S2 and S3).

Figure 2b shows energy differences of the competing intermediates. It is notable that the CO_2R reaction is predicted to favor pathway 2 or 3 over pathway 1 in most TMDs, showing G^0(*COOH) > G^0(*OCHO). This also results from the steric hindrance. Meanwhile, in tellurides such as $TaTe_2$, $NiTe_2$, and WTe_2, *COOH and *OCHO display similar energies such that these materials might exhibit no clear preference among the pathways. In addition, in $ReTe_2$, $IrTe_2$, and PtS_2, *COOH shows lower free energies than *OCHO. This is attributed to their large lattice parameters (>3.6 Å), which weakens the steric hindrance of V_X. We further compare G^0(*+HCOOH(aq)) and G^0(*O + HCHO(aq)) to identify the preference between pathway 2 and 3. This comparison shows that pathway 3 can be a main CO_2R route in the

majority of TMDs. This fact stems from the strong binding of oxygen to the transition metal at the vacancy site,[17,51] generally resulting in lower energies of *O + HCHO(aq) than *+HCOOH(aq) at V_X in TMDs.

Hereafter, TMDs in which the CO_2R reaction prefers Pathway N will be classified as Type N. As stated in the foregoing discussion, a clear-cut classification may be difficult for some TMDs due to similar energies between competing intermediates. Furthermore, PBE was reported to have some errors in describing surface reactions (Figure S4).[52] Considering these facts, if the magnitude of the energy difference between competing intermediates is less than 0.2 eV, we classify TMDs to include in both types.

Next, we assess the theoretical onset potential (U_{onset}) and the selectivity of the CO_2R reaction against the HER of TMD catalysts. The U_{onset} is evaluated as the least-negative electrode potential at which the reaction free energy of every reaction step becomes negative.[30,32] The selectivity between CO_2R and the HER is determined by the free-energy difference of the first reaction intermediates of CO_2R and HER at U_{onset} (ΔG_{sel}), i.e., $\Delta G_{sel} = G^{U_{onset}}$(*COOH) − $G^{U_{onset}}$(*H) for pathway 1 and $\Delta G_{sel} = G^{U_{onset}}$(*OCHO) − $G^{U_{onset}}$(*H) for pathways 2 and 3, in line with previous calculations.[17,49,53,54] In Figure 3a−c, ΔG_{sel}'s at U_{onset} are presented for Type 1−3 TMDs, respectively. In these plots, materials that appear in the bottom left of the figure are more promising catalysts. For comparison purpose, we also mark the calculated values on Au(111), Sn(100), and Cu(111), which are well-known CO_2R catalysts producing CO, HCOOH, and highly reduced species,
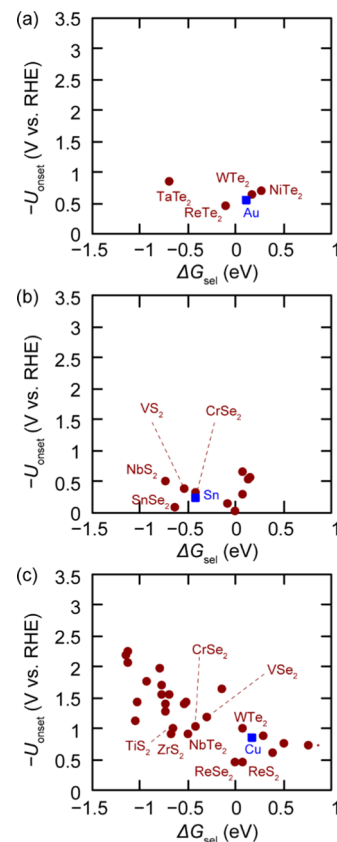
Figure 3. Distribution of ΔG_{sel} and $-U_{onset}$ of TMD catalysts for (a) pathway 1, (b) pathway 2, and (c) pathway 3. The materials that appear in the bottom left are more promising.
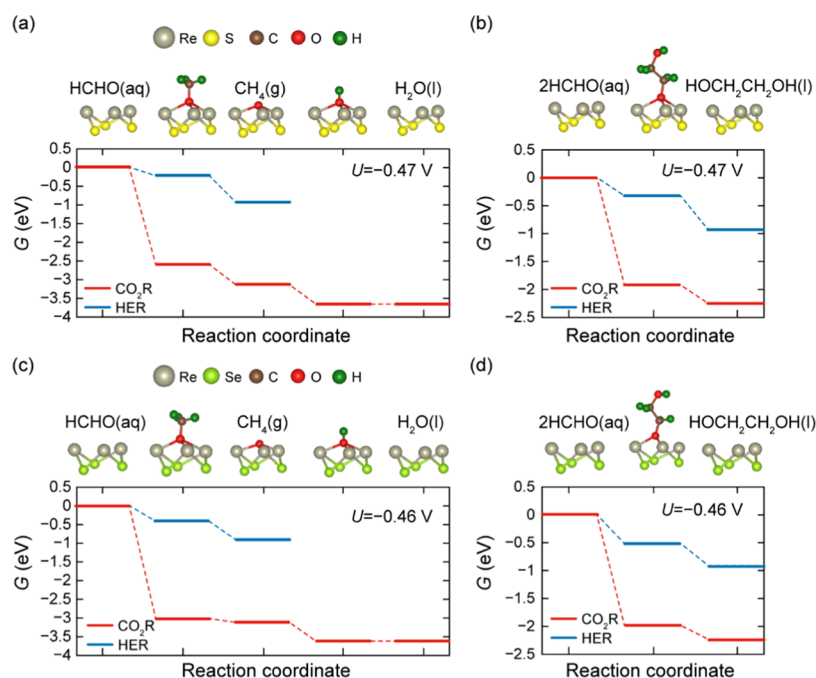
Figure 4. Free-energy diagrams for the (a) C_1 pathway to methane and (b) C_2 pathway to ethylene glycol of ReS_2. Free-energy diagrams for the (c) C_1 pathway to methane and (d) C_2 pathway to ethylene glycol of $ReSe_2$.

respectively, in Figure 3. Several TMDs such as MoS_2, PtS_2, $PtSe_2$, $PtTe_2$, and $IrTe_2$ are omitted in Figure 3 because the reaction free energy of the initial protonation step, namely, $G^U(*OCHO)$ or $G^U(*COOH)$, always remains positive at any U. This happens due to a more negative charge state of pure V_X than that of *OCHO or *COOH in those materials (see Figure S1).[17] Note that uniformly positive reaction energies in the initial reduction of CO_2 would indicate unfavorable CO_2R selectivity against the HER as well as low faradic efficiencies. Indeed, it was reported that MoS_2 suffers from poor selectivity and low faradic efficiency in CO_2R.[16]

Among Type 1 TMDs, we find that $ReTe_2$, $TaTe_2$, $NiTe_2$, and WTe_2 are promising CO_2R catalysts (Figure 3a). In particular, ΔG_{sel} of $TaTe_2$ is much lower than that of Au, implying $TaTe_2$ is advantageous over Au in terms of the CO_2R selectivity. On the other hand, $SnSe_2$, VS_2, and NbS_2 are notable among Type 2 TMDs, showing U_{onset} of -0.09, -0.39, and -0.49 V and ΔG_{sel} of -0.54, -0.43, and -0.63 V, respectively. These values are more favorable than those of Sn (Figure 3b). This finding is consistent with the recent experiments where $SnSe_2$ catalysts produce HCOOH as the main product at negatively small onset potentials (> -0.5 V) with high faradic efficiencies ($\sim 90\%$) and good stability during the reactions.[55,56] Among Type 3 TMDs, the ΔG_{sel} and U_{onset} values of several TMDs such as ReS_2, $ReSe_2$, WTe_2, $CrSe_2$, and VSe_2 are on par with those of Cu. In particular, ReS_2 and $ReSe_2$ are of interest more than the others because they are predicted to be superior to Cu. Furthermore, these materials are known to be stable under reduction environments.[57−59] We also confirm the stability of the candidate materials, namely, $SnSe_2$, ReS_2, and $ReSe_2$, by calculating oxidation/reduction leaching potential (Figure S5).[60]

3.2. C_N Pathways in ReS_2 and $ReSe_2$. Pathways to highly reduced species can open due to the resorption of HCHO produced via pathway 3. For instance, the HCHO reduction was also proposed as an important mechanism for CO_2R

catalysts such as MoS_2,[17] Cu-CNT,[61] Cu foil,[62] and Fe−N−C.[63] In this subsection, we examine free-energy diagrams for C_1 pathways to methane and methanol and C_2 pathways to ethylene glycol ($HOCH_2CH_2OH$) in ReS_2 and $ReSe_2$, to check whether such pathways can indeed open. These CO_2R products were reported to be generated on MoS_2 electrodes even if their faradic efficiencies were low,[16] and the plausible pathways for them were suggested based on resorption of HCHO at active sites in previous calculations.[17] However, it should be kept in mind that there can be various possible pathways to C_N species starting from the HCHO resorption that are thermodynamically favorable, and it is challenging to predict a major product without detailed analysis of reaction kinetics.[17] Figure 4a,c shows the free energies and atomic structures of intermediates for the C_1 pathways to CH_4 in ReS_2 and $ReSe_2$, respectively. In both catalysts, every protonation step is downhill in energy at U_{onset} that opens pathway 3. Thus, these pathways are feasible. In the case of the C_1 pathways to CH_3OH, it is less favorable than that for CH_4, but can also open in both materials (Figure S6). In Figure 4b,d, we plot the free energies and atomic structures of intermediates for the C_2 pathways to $HOCH_2CH_2OH$ in ReS_2 and $ReSe_2$, respectively. It turns out that the protonation of the dimerized HCHO molecule at active sites in these materials, namely, 2HCHO → $*OCH_2CH_2OH$ → $HOCH_2CH_2OH$, is also downhill in energy at the U_{onset} for pathway 3. Therefore, these pathways are viable. (Herein, we focus on the protonation steps within the CHE model for the C_2 pathways, but the actual reactions are likely to entail more complicated reaction steps based on the Langmuir−Hinshelwood or Eley−Rideal mechanism.[64] Detailed mechanisms for the HCHO condensation will be investigated in our future study.) Among the C_1 and C_2 pathways examined in this subsection, we find the pathway to CH_4 to be most thermodynamically favorable. Interestingly, we see that the C_1 and C_2 pathways are largely preferred over the HER in energy. This may imply that there are few
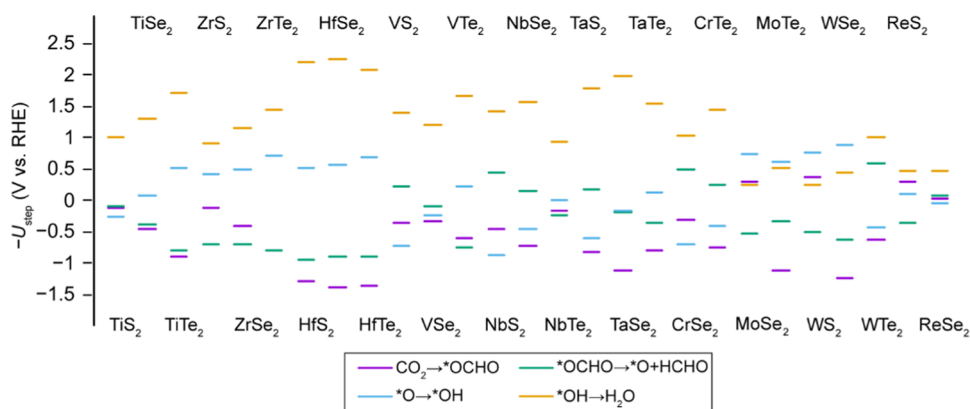
Figure 5. Limiting potentials of each reaction step of the CO_2R pathway to HCHO (pathway 3).

selectivity issues of CO_2R against the HER for the following C_N pathways, once HCHO is produced as a primary C_1 product on a given TMD catalyst.

3.3. Simple Descriptor for Predicting HCHO Production. As mentioned above, highly reduced chemical species that can evolve from the HCHO reduction (e.g., methanol, ethylene glycol, and 1-propanol) as well as HCHO itself are highly valuable practically.[2,3] Therefore, identifying simple descriptors for the onset potential of pathway 3 is highly desirable, which will help design CO_2R catalysts capable of producing high-value species. To find such descriptors, we first reveal which reaction step contributes to U_{onset} in Type 3 TMDs. Figure 5 shows that the limiting potential at which the reaction free energy becomes 0 eV for each step in pathway 3 (U_{step}). In most Type 3 TMDs, the limiting step with the largest negative U_{step}, i.e., U_{onset}, occurs at the reaction step of *OH → H_2O. Exceptions are $MoSe_2$, $MoTe_2$, WS_2, and WSe_2, wherein the potential limiting step appears at *O → *OH. This is attributed to an increase in q during the reaction process of *O → *OH in these materials (see Table S2).

Since the potential limiting step mostly occurs at *OH → H_2O, it would be reasonable to choose $G^0(*OH)$ as a descriptor for onset potentials. However, we find that $G^0(*OCHO)$ linearly correlates with $G^0(*OH)$, as shown in Figure 6a. Such a linear relation would arise from the fact that the adsorbates, namely, *OH and *OCHO, involve M−O bonds. Since $G^0(*OCHO)$ can be used to assess the selectivity of CO_2R over the HER by directly comparing with $G^0(*H)$, we select $G^0(*OCHO)$ as the descriptor. In Figure 6b, we present $-U_{onset}$ with respect to $G^0(*OCHO)$ for 23 Type 3 TMDs where the potential limiting step occurs at *OH → H_2O, which shows a good scaling relation between them.

We find a volcanic behavior of the scaling relation wherein the minimum value of $-U_{onset}$ is about 0.2 V at $G^0(*OCHO)$ = 0.2 eV (Figure 6b). This minimum of $-U_{onset}$ is smaller than that for CO_2R on typical transition metals.[65] The volcano relation can be explained as follows: at large, negative $G^0(*OCHO)$, *OH is stable so that the formation of H_2O is difficult, yielding a large $-U_{onset}$. In contrast, as $G^0(*OCHO)$ positively grows, the limiting potential for the reduction of *OH declines, but at the same time, the initial reduction of CO_2 to form *OCHO becomes more difficult. As a result, the formation of *OCHO can become a potential limiting step at large $G^0(*OCHO)$, although most of TMDs considered in the present work lead to *OH → H_2O as the limiting step. Note that, in ReS_2 wherein $G^0(*OCHO)$ is close to 0.2 eV, the
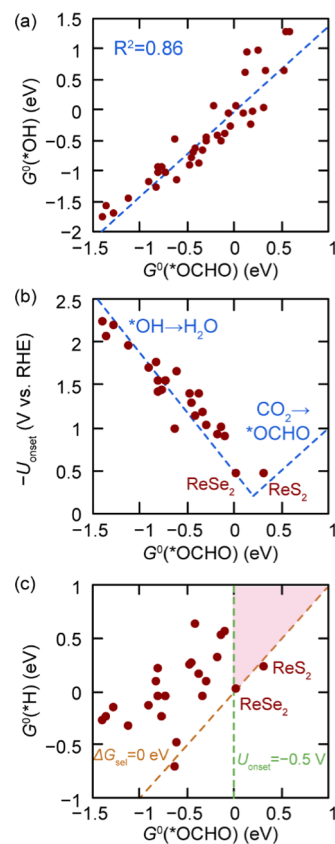
Figure 6. (a) Scaling relation between $G^0(*OCHO)$ and $G^0(*OH)$. (b) Volcano plot of $-U_{onset}$ as a function of $G^0(*OCHO)$. (c) Distribution of $G^0(*OCHO)$ and $G^0(*H)$ in Type 3 TMDs. The shaded area represents the sweet spot for $-U_{onset} < 0.5$ V and $\Delta G_{sel} < 0$ eV.

$-U_{step}$ values for *OH → H_2O and * + CO_2 → *OCHO are indeed similar to each other (Figure 5). The inconsistency between the location of the data of ReS_2 in the volcano plot and the actual potential limiting step arises from the incomplete scaling relation between $G^0(*OH)$ and $G^0(*OCHO)$ (the volcano plot based on $G^0(*OH)$ is shown in Figure S7). Based on the volcano plot in Figure 6b, we graphically present the free-energy conditions for choosing good CO_2R TMD catalysts in Figure 6c. The shaded region represents the sweet spot wherein the catalysts are expected to show $U_{onset} > -0.5$ V and $\Delta G_{sel} < 0$ eV. The promising

candidates such as ReS_2 and $ReSe_2$ appear very close to the sweet spot, indicating that our descriptors are valid.

3.4. Electronic Structure of *OCHO. To gain chemical insights into the free energy of *OCHO in type 3 TMDs, we analyze the electronic structure of *OCHO. In Figure 7a, we
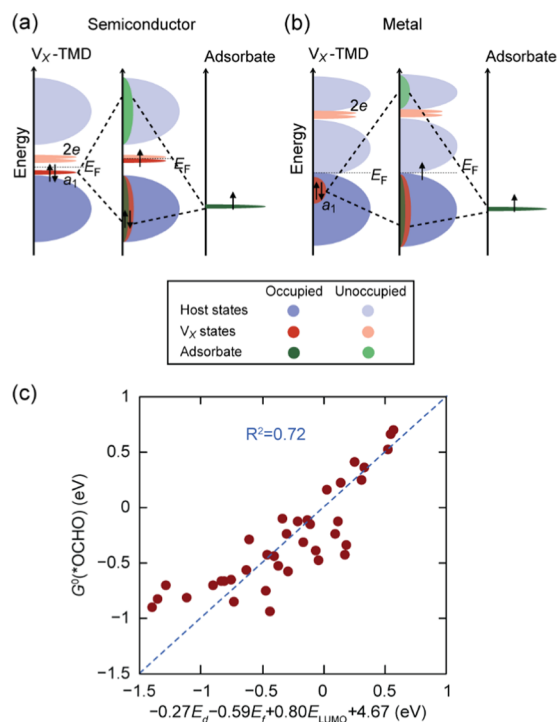
Figure 7. Schematic band diagrams illustrating the interaction between *OCHO and V_X of (a) semiconducting TMDs with midgap states and (b) metallic TMDs. (c) Regression result showing the correlation between G^0(*OCHO) and physical parameters such as E_d, E_f, and E_{LUMO}.

present a schematic band diagram illustrating the interaction between OCHO and V_X in semiconducting TMDs (see the calculated density of states in Figure S8). In TMDs with vacancies (V_X-TMDs), the hybridization among the dangling bonds of cations adjacent to V_X develops three defect levels: one a_1 state and two degenerate e states. When OCHO is adsorbed, the lower a_1 state reacts with the frontier state of OCHO, which results in bonding and antibonding states. In the case of the bonding state, its level appears below the highest occupied molecular orbital (HOMO) level of V_X-TMDs and is occupied with two electrons. In contrast, the antibonding state lies above the lowest unoccupied molecular orbital (LUMO) level (E_{LUMO}) of V_X-TMDs. Accordingly, the antibonding level remains empty in *OCHO. Like semiconducting TMDs, the hybridization between the a_1 state in metallic V_X-TMDs and the HOMO level of OCHO produces the occupied bonding state below the HOMO of the V_X-TMDs, while the unoccupied antibonding state lies above the Fermi level (Figure 7b).

With the insights obtained from the analysis of the electronic structure above, we identify key materials properties that affect G^0(*OCHO). The first one is the position of the d band of cations of TMDs, which is typically represented by the d-band center (E_d). Because the vacancy states in V_X-TMDs consist of d orbitals of cations adjacent to the vacancy site, the energy of the a_1 state increases with E_d. As a result, a larger decrease in

energy can be obtained by the electron transfer from the a_1 state to the bonding state upon the OCHO adsorption as E_d increases. Therefore, E_d has a negative correlation with G^0(*OCHO). Next, the LUMO level of V_X-TMDs accepts the excess electron after occupying the bonding state. Thus, G^0(*OCHO) decreases with the E_{LUMO} of V_X-TMDs. Note that LUMO of V_X-TMDs, in particular, metallic or semiconducting systems without localized states in the gap, is formed by the hybridization between cation and anion states. Thus, E_{LUMO} does not solely depend on E_d in general. Finally, another important factor is the vacancy formation energy that can be a measure of the stability of V_X. Thus, higher E_f indicates a larger energy loss associated with breaking bonds between cations and OCHO at active sites. To corroborate the correlation of the three materials parameters, namely, E_d, E_{LUMO}, and E_f, with G^0(*OCHO), the G^0(*OCHO) data are fitted by multiple linear regression scheme using such factors as independent variables (Figure 7c). The result shows that G^0(*OCHO) is indeed reasonably well described by these factors. Note that, unlike transition-metal catalysts, E_d alone cannot describe free energies of adsorbates in V_X-TMDs (see Figure S9).

4. CONCLUSIONS

In conclusion, we have explored the CO_2R activity of anion vacancies of the 38 TMDs using first-principles calculations. The majority of TMDs are predicted to produce HCHO that acts as a source to evolve highly reduced species with larger economic benefits due to steric hindrance of V_X. Several TMDs such as ReS_2 and $ReSe_2$ are selected as promising CO_2R catalysts, which are expected to have both low overpotential and high selectivity. To gain more insight into the HCHO pathway, we have analyzed potential limiting steps of CO_2R reactions, suggesting that the free energy of *OCHO and *H can be good descriptors for the CO_2R activity and selectivity. Since the preference of the HCHO formation originates from the geometrical constraints at V_X, which leads to steric hindrance, our analysis and the descriptors are universally applicable to evaluating the catalytic performance of other compounds with vacancies as active sites. Accordingly, the present study will also contribute to discovering novel catalysts that can efficiently produce high-value chemicals from CO_2.

■ ASSOCIATED CONTENT

ⓢ Supporting Information

The Supporting Information is available free of charge at https://pubs.acs.org/doi/10.1021/acs.jpcc.0c07113.

> Derivation of the main equation, all free energies of TMDs, geometry of adsorbates, density of states of representative materials, and d-band center fitting results (PDF)

■ AUTHOR INFORMATION

Corresponding Author

Youngho Kang − *Department of Materials Science and Engineering, Incheon National University, Incheon 22012, Korea;* ⓞ orcid.org/0000-0003-4532-0027; Email: youngho84@inu.ac.kr

Authors

Sungwoo Kang − *Department of Materials Science and Engineering, Seoul National University, Seoul 08826, Korea;*
orcid.org/0000-0001-8177-8815

Suyeon Ju − *Department of Materials Science and Engineering, Seoul National University, Seoul 08826, Korea;*
orcid.org/0000-0001-7033-8769

Seungwu Han − *Department of Materials Science and Engineering, Seoul National University, Seoul 08826, Korea;*
orcid.org/0000-0003-3958-0922

Complete contact information is available at:
https://pubs.acs.org/10.1021/acs.jpcc.0c07113

Notes

The authors declare no competing financial interest.

■ REFERENCES

(1) Greenblatt, J. B.; Miller, D. J.; Ager, J. W.; Houle, F. A.; Sharp, I. D. The Technical and Energetic Challenges of Separating (Photo)-Electrochemical Carbon Dioxide Reduction Products. *Joule* **2018**, *2*, 381−420.

(2) Lu, Q.; Jiao, F. Electrochemical CO_2 Reduction: Electrocatalyst, Reaction Mechanism, and Process Engineering. *Nano Energy* **2016**, *29*, 439−456.

(3) Jouny, M.; Luc, W. W.; Jiao, F. A General Techno-Economic Analysis of CO_2 Electrolysis Systems. *Ind. Eng. Chem. Res.* **2018**, *57*, 2165−2177.

(4) Bushuyev, O. S.; De Luna, P.; Dinh, C. T.; Tao, L.; Saur, G.; van de Lagemaat, J.; Kelley, S. O.; Sargent, E. H. What Should We Make with CO_2 and How Can We Make It? *Joule* **2018**, *2*, 825−832.

(5) Song, Y.; Peng, R.; Hensley, D. K.; Bonnesen, P. V.; Liang, L.; Wu, Z.; Meyer, H. M.; Chi, M.; Ma, C.; Sumpter, B. G.; Rondinone, A. J. High-Selectivity Electrochemical Conversion of CO_2 to Ethanol Using a Copper Nanoparticle/N-Doped Graphene Electrode. *ChemistrySelect* **2016**, *1*, 6055−6061.

(6) Kaneco, S.; Katsumata, H.; Suzuki, T.; Ohta, K. Electrochemical Reduction of CO_2 to Methane at the Cu Electrode in Methanol with Sodium Supporting Salts and Its Comparison with Other Alkaline Salts. *Energy Fuels* **2006**, *20*, 409−414.

(7) Varela, A. S.; Ju, W.; Reier, T.; Strasser, P. Tuning the Catalytic Activity and Selectivity of Cu for CO_2 Electroreduction in the Presence of Halides. *ACS Catal.* **2016**, *6*, 2136−2144.

(8) Lum, Y.; Ager, J. W. Evidence for Product-Specific Active Sites on Oxide-Derived Cu Catalysts for Electrochemical CO_2 Reduction. *Nat. Catal.* **2019**, *2*, 86−93.

(9) Calvinho, K. U. D.; Laursen, A. B.; Yap, K. M. K.; Goetjen, T. A.; Hwang, S.; Murali, N.; Mejia-Sosa, B.; Lubarski, A.; Teeluck, K. M.; Hall, E. S.; et al. Selective CO_2 Reduction to C_3 and C_4 Oxyhydrocarbons on Nickel Phosphides at Overpotentials as Low as 10 mV. *Energy Environ. Sci.* **2018**, *11*, 2550−2559.

(10) Hinnemann, B.; Moses, P. G.; Bonde, J.; Jørgensen, K. P.; Nielsen, J. H.; Horch, S.; Chorkendorff, I.; Nørskov, J. K. Biomimetic Hydrogen Evolution: MoS_2 Nanoparticles as Catalyst for Hydrogen Evolution. *J. Am. Chem. Soc.* **2005**, *127*, 5308−5309.

(11) Jaramillo, T. F.; Jorgensen, K. P.; Bonde, J.; Nielsen, J. H.; Horch, S.; Chorkendorff, I. Identification of Active Edge Sites for Electrochemical H_2 Evolution from MoS_2 Nanocatalysts. *Science* **2007**, *317*, 100−102.

(12) Andoshe, D. M.; Jeon, J. M.; Kim, S. Y.; Jang, H. W. Two-Dimensional Transition Metal Dichalcogenide Nanomaterials for Solar Water Splitting. *Electron. Mater. Lett.* **2015**, *11*, 323−335.

(13) Deng, D.; Novoselov, K. S.; Fu, Q.; Zheng, N.; Tian, Z.; Bao, X. Catalysis with Two-Dimensional Materials and Their Heterostructures. *Nat. Nanotechnol.* **2016**, *11*, 218−230.

(14) Lee, J.; Kang, S.; Yim, K.; Kim, K.; Jang, H. W.; Kang, Y.; Han, S. Hydrogen Evolution Reaction at Anion Vacancy of Two-Dimensional Transition Metal Dichalcogenides: Ab Initio Computational Screening. *J. Phys. Chem. Lett.* **2018**, *9*, 2049−2055.

(15) Ji, Y.; Nørskov, J. K.; Chan, K. Scaling Relations on Basal Plane Vacancies of Transition Metal Dichalcogenides for CO_2 Reduction. *J. Phys. Chem. C* **2019**, *123*, 4256−4261.

(16) Francis, S. A.; Velazquez, J. M.; Ferrer, I. M.; Torelli, D. A.; Guevarra, D.; McDowell, M. T.; Sun, K.; Zhou, X.; Saadi, F. H.; John, J.; et al. Reduction of Aqueous CO_2 to 1-Propanol at MoS_2 Electrodes. *Chem. Mater.* **2018**, *30*, 4902−4908.

(17) Kang, S.; Han, S.; Kang, Y. Unveiling Electrochemical Reaction Pathways of CO_2 Reduction to C_N Species at S-Vacancies of MoS_2. *ChemSusChem* **2019**, *12*, 2671−2678.

(18) Wang, S.; Robertson, A.; Warner, J. H. Atomic Structure of Defects and Dopants in 2D Layered Transition Metal Dichalcogenides. *Chem. Soc. Rev.* **2018**, *47*, 6764−6794.

(19) Hildebrand, B.; Didiot, C.; Novello, A. M.; Monney, G.; Scarfato, A.; Ubaldini, A.; Berger, H.; Bowler, D. R.; Renner, C.; Aebi, P. Doping Nature of Native Defects in 1T-$TiSe_2$. *Phys. Rev. Lett.* **2014**, *112*, No. 197001.

(20) Huang, J.; Gao, H.; Xia, Y.; Sun, Y.; Xiong, J.; Li, Y.; Cong, S.; Guo, J.; Du, S.; Zou, G. Enhanced Photoelectrochemical Performance of Defect-Rich ReS_2 Nanosheets in Visible-Light Assisted Hydrogen Generation. *Nano Energy* **2018**, *46*, 305−313.

(21) Avsar, A.; Ciarrocchi, A.; Pizzochero, M.; Unuchek, D.; Yazyev, O. V.; Kis, A. Defect Induced, Layer-Modulated Magnetism in Ultrathin Metallic $PtSe_2$. *Nat. Nanotechnol.* **2019**, *14*, 674−678.

(22) Lin, Z.; Carvalho, B. R.; Kahn, E.; Lv, R.; Rao, R.; Terrones, H.; Pimenta, M. A.; Terrones, M. Defect Engineering of Two-Dimensional Transition Metal Dichalcogenides. *2D Mater.* **2016**, *3*, No. 022002.

(23) Li, X.; Puretzky, A. A.; Sang, X.; KC, S.; Tian, M.; Ceballos, F.; Mahjouri-samani, M.; Wang, K.; Unocic, R. R.; Zhao, H.; et al. Suppression of Defects and Deep Levels Using Isoelectronic Tungsten Substitution in Monolayer $MoSe_2$. *Adv. Funct. Mater.* **2017**, *27*, No. 1603850.

(24) Lin, Y.-C.; Li, S.; Komsa, H.; Chang, L.; Krasheninnikov, A. V.; Eda, G.; Suenaga, K. Revealing the Atomic Defects of WS_2 Governing Its Distinct Optical Emissions. *Adv. Funct. Mater.* **2018**, *28*, No. 1704210.

(25) Nguyen, L.; Komsa, H. P.; Khestanova, E.; Kashtiban, R. J.; Peters, J. J. P.; Lawlor, S.; Sanchez, A. M.; Sloan, J.; Gorbachev, R. V.; Grigorieva, I. V.; et al. Atomic Defects and Doping of Monolayer $NbSe_2$. *ACS Nano* **2017**, *11*, 2894−2904.

(26) Zhang, Y.; Chen, X.; Huang, Y.; Zhang, C.; Li, F.; Shu, H. The Role of Intrinsic Defects in Electrocatalytic Activity of Monolayer VS_2 Basal Planes for the Hydrogen Evolution Reaction. *J. Phys. Chem. C* **2017**, *121*, 1530−1536.

(27) Li, H.; Tsai, C.; Koh, A. L.; Cai, L.; Contryman, A. W.; Fragapane, A. H.; Zhao, J.; Han, H. S.; Manoharan, H. C.; Abild-Pedersen, F.; et al. Activating and Optimizing MoS_2 Basal Planes for Hydrogen Evolution through the Formation of Strained Sulphur Vacancies. *Nat. Mater.* **2016**, *15*, 48−53.

(28) Tsai, C.; Li, H.; Park, S.; Park, J.; Han, H. S.; Nørskov, J. K.; Zheng, X.; Abild-Pedersen, F. Electrochemical Generation of Sulfur Vacancies in the Basal Plane of MoS_2 for Hydrogen Evolution. *Nat. Commun.* **2017**, *8*, No. 15113.

(29) Nam, D. H.; Kim, J. Y.; Kang, S.; Joo, W.; Lee, S. Y.; Seo, H.; Kim, H. G.; Ahn, I. K.; Lee, G. B.; Choi, M.; et al. Anion Extraction-Induced Polymorph Control of Transition Metal Dichalcogenides. *Nano Lett.* **2019**, *19*, 8644−8652.

(30) Nørskov, J. K.; Rossmeisl, J.; Logadottir, A.; Lindqvist, L.; Kitchin, J. R.; Bligaard, T.; Jónsson, H. Origin of the Overpotential for Oxygen Reduction at a Fuel-Cell Cathode. *J. Phys. Chem. B* **2004**, *108*, 17886−17892.

(31) Kim, K. Y.; Lee, J.; Kang, S.; Son, Y.-W.; Jan, H. W.; Kang, Y.; Han, S. Role of Hyper-Reduced States in Hydrogen Evolution Reaction at Sulfur Vacancy in MoS_2. *ACS Catal.* **2018**, *8*, 4508−4515.

(32) Peterson, A. A.; Abild-Pedersen, F.; Studt, F.; Rossmeisl, J.; Nørskov, J. K. How Copper Catalyzes the Electroreduction of Carbon Dioxide into Hydrocarbon Fuels. *Energy Environ. Sci.* **2010**, *3*, 1311−1315.

(33) Zhao, X.; Liu, Y. Unveiling the Active Structure of Single Nickel Atom Catalysis: Critical Roles of Charge Capacity and Hydrogen Bonding. *J. Am. Chem. Soc.* **2020**, *142*, 5773−5777.

(34) Chen, X.; Gu, Y.; Tao, G.; Pei, Y.; Wang, G.; Cui, N. Origin of Hydrogen Evolution Activity on MS_2 (M = Mo or Nb) Monolayers. *J. Mater. Chem. A* **2015**, *3*, 18898−18905.

(35) Hong, X.; Chan, K.; Tsai, C.; Nørskov, J. K. How Doped MoS_2 Breaks Transition-Metal Scaling Relations for CO_2 Electrochemical Reduction. *ACS Catal.* **2016**, *6*, 4428−4437.

(36) Afeefy, H.; Liebman, J.; Stein, S. Neutral Thermodynamical Data. In *NIST CheistryWebBook, NIST Standard Reference Database Number 69*; Linstrom, P. J.; Mallard, W. G., Eds.; National institute of Standards and Technology: Gaithersburg, MD, 2018; p 20899.

(37) Kresse, G.; Furthmüller, J. Efficient Iterative Schemes for Ab Initio Total-Energy Calculations Using a Plane-Wave Basis Set. *Phys. Rev. B* **1996**, *54*, 11169−11186.

(38) Perdew, J. P.; Burke, K.; Ernzerhof, M. Generalized Gradient Approximation Made Simple. *Phys. Rev. Lett.* **1996**, *77*, 3865−3868.

(39) Mathew, K.; Sundararaman, R.; Letchworth-Weaver, K.; Arias, T. A.; Hennig, R. G. Implicit Solvation Model for Density-Functional Study of Nanocrystal Surfaces and Reaction Pathways. *J. Chem. Phys.* **2014**, *140*, No. 084106.

(40) Grimme, S. Semiempirical GGA-Type Density Functional Constructed with a Long-Range Dispersion Correction. *J. Comput. Chem.* **2006**, *27*, 1787−1799.

(41) Pourbaix, M. J. N. *Atlas D'equilibres Electrochimiques*; Gauthier-Villars, Paris, 1963.

(42) Hellenbrandt, M. The Inorganic Crystal Structure Database (ICSD) - Present and Future. *Crystallogr. Rev.* **2004**, *10*, 17−22.

(43) Xiao, H.; Cheng, T.; Goddard, W. A.; Sundararaman, R. Mechanistic Explanation of the PH Dependence and Onset Potentials for Hydrocarbon Products from Electrochemical Reduction of CO on Cu (111). *J. Am. Chem. Soc.* **2016**, *138*, 483−486.

(44) Schouten, K. J. P.; Kwon, Y.; van der Ham, C. J. M.; Qin, Z.; Koper, M. T. M. A New Mechanism for the Selectivity to C_1 and C_2 Species in the Electrochemical Reduction of Carbon Dioxide on Copper Electrodes. *Chem. Sci.* **2011**, *2*, 1902−1909.

(45) Montoya, J. H.; Peterson, A. A.; Nørskov, J. K. Insights into C-C Coupling in CO_2 Electroreduction on Copper Electrodes. *ChemCatChem* **2013**, *5*, 737−742.

(46) Hanselman, S.; Koper, M. T. M.; Calle-Vallejo, F. Computational Comparison of Late Transition Metal (100) Surfaces for the Electrocatalytic Reduction of CO to C_2 Species. *ACS Energy Lett.* **2018**, *3*, 1062−1067.

(47) Karamad, M.; Hansen, H. A.; Rossmeisl, J.; Nørskov, J. K. Mechanistic Pathway in the Electrochemical Reduction of CO_2 on RuO_2. *ACS Catal.* **2015**, *5*, 4075−4081.

(48) Tayyebi, E.; Hussain, J.; Abghoui, Y.; Skúlason, E. Trends of Electrochemical CO_2 Reduction Reaction on Transition Metal Oxide Catalysts. *J. Phys. Chem. C* **2018**, *122*, 10078−10087.

(49) Varley, J. B.; Hansen, H. A.; Ammitzbøll, N. L.; Grabow, L. C.; Peterson, A. A.; Rossmeisl, J.; Nørskov, J. K. Ni−Fe−S Cubanes in CO_2 Reduction Electrocatalysis: A DFT Study. *ACS Catal.* **2013**, *3*, 2640−2643.

(50) Chen, Z. W.; Gao, W.; Zheng, W. T.; Jiang, Q. Steric Hindrance in Sulfur Vacancy of Monolayer MoS_2 Boosts Electrochemical Reduction of Carbon Monoxide to Methane. *ChemSusChem* **2018**, *11*, 1455−1459.

(51) Sen, H. S.; Sahin, H.; Peeters, F. M.; Durgun, E. Monolayers of MoS_2 as an Oxidation Protective Nanocoating Material. *J. Appl. Phys.* **2014**, *116*, No. 083508.

(52) Wellendorff, J.; Lundgaard, K. T.; Møgelhøj, A.; Petzold, V.; Landis, D. D.; Nørskov, J. K.; Bligaard, T.; Jacobsen, K. W. Density Functionals for Surface Science: Exchange-Correlation Model Development with Bayesian Error Estimation. *Phys. Rev. B* **2012**, *85*, No. 235149.

(53) Cui, X.; An, W.; Liu, X.; Wang, H.; Men, Y.; Wang, J. C_2N-Graphene Supported Single-Atom Catalysts for CO_2 Electrochemical Reduction Reaction: Mechanistic Insight and Catalyst Screening. *Nanoscale* **2018**, *10*, 15262−15272.

(54) Back, S.; Jung, Y. TiC- and TiN-Supported Single-Atom Catalysts for Dramatic Improvements in CO_2 Electrochemical Reduction to CH_4. *ACS Energy Lett.* **2017**, *2*, 969−975.

(55) Yang, H.; Liu, H.; Liu, X.; Zhao, Z.; Luo, J. Electroreduction of Carbon Dioxide to Formate over a Thin-Layered Tin Diselenide Electrode. *Catal. Sci. Technol.* **2018**, *8*, 5428−5433.

(56) He, B.; Jia, L.; Cui, Y.; Zhou, W.; Sun, J.; Xu, J.; Wang, Q.; Zhao, L. $SnSe_2$ Nanorods on Carbon Cloth as a Highly Selective, Active, and Flexible Electrocatalyst for Electrochemical Reduction of CO_2 into Formate. *ACS Appl. Energy Mater.* **2019**, *2*, 7655−7662.

(57) Fujita, T.; Ito, Y.; Tan, Y.; Yamaguchi, H.; Hojo, D.; Hirata, A.; Voiry, D.; Chhowalla, M.; Chen, M. Chemically Exfoliated ReS_2 Nanosheets. *Nanoscale* **2014**, *6*, 12458−12462.

(58) Majidi, L.; Hemmat, Z.; Warburton, R. E.; Kumar, K.; Ahmadiparidari, A.; Hong, L.; Guo, J.; Zapol, P.; Klie, R. F.; Cabana, J.; et al. Highly Active Rhenium-, Ruthenium-, and Iridium-Based Dichalcogenide Electrocatalysts for Oxygen Reduction and Oxygen Evolution Reactions in Aprotic Media. *Chem. Mater.* **2020**, *32*, 2764−2773.

(59) Qi, F.; Wang, X.; Zheng, B.; Chen, Y.; Yu, B.; Zhou, J.; He, J.; Li, P.; Zhang, W.; Li, Y. Self-Assembled Chrysanthemum-like Microspheres Constructed by Few-Layer $ReSe_2$ Nanosheets as a Highly Efficient and Stable Electrocatalyst for Hydrogen Evolution Reaction. *Electrochim. Acta* **2017**, *224*, 593−599.

(60) Shin, H.; Ha, Y.; Kim, H. 2D Covalent Metals: A New Materials Domain of Electrochemical CO_2 Conversion with Broken Scaling Relationship. *J. Phys. Chem. Lett.* **2016**, *7*, 4124−4129.

(61) Genovese, C.; Ampelli, C.; Perathoner, S.; Centi, G. Mechanism of C−C Bond Formation in the Electrocatalytic Reduction of CO_2 to Acetic Acid. A Challenging Reaction to Use Renewable Energy with Chemistry. *Green Chem.* **2017**, *19*, 2406−2415.

(62) Kim, C. W.; Kang, M. J.; Ji, S.; Kang, Y. S. Artificial Photosynthesis for Formaldehyde Production with 85% of Faradaic Efficiency by Tuning the Reduction Potential. *ACS Catal.* **2018**, *8*, 968−974.

(63) Ju, W.; Bagger, A.; Wang, X.; Tsai, Y.; Luo, F.; Möller, T.; Wang, H.; Rossmeisl, J.; Varela, A. S.; Strasser, P. Unraveling Mechanistic Reaction Pathways of the Electrochemical CO_2 Reduction on Fe-N-C Single-Site Catalysts. *ACS Energy Lett.* **2019**, *4*, 1663−1671.

(64) Kolasinski, K. W. *Surface Science: Foundations of Catalysis and Nanoscience*; John Wiley & Sons: New York, 2012.

(65) Peterson, A. A.; Nørskov, J. K. Activity Descriptors for CO_2 Electroreduction to Methane on Transition-Metal Catalysts. *J. Phys. Chem. Lett.* **2012**, *3*, 251−258.